This article has been accepted for publication in a future issue of this journal, but has not been fully edited. Content may change prior to final publication. Citation information: DOI 10.1109/TMI.2015.2479455, IEEE Transactions on Medical Imaging

Unifying concepts of statistical and spectral quantitative ultrasound techniques

François Destrempes, Emilie Franceschini, François T. H. Yu, Guy Cloutier

***Abstract*—Quantitative ultrasound (QUS) techniques using radiofrequency (RF) backscattered signals have been used for tissue characterization of numerous organ systems. One approach is to use the magnitude and frequency dependence of backscatter echoes to quantify tissue structures. Another approach is to use first-order statistical properties of the echo envelope as a signature of the tissue microstructure. We propose here a unification of these QUS concepts. For this purpose, a mixture of homodyned K-distributions is introduced to model the echo envelope, together with an estimation method and a physical interpretation of its parameters based on the echo signal spectrum. In particular, the total, coherent and diffuse signal powers related to the proposed mixture model are expressed explicitly in terms of the structure factor previously studied to describe the backscatter coefficient (BSC). Then, this approach is illustrated in the context of red blood cell (RBC) aggregation. In this context, the structure factor intervenes due to the aggregation of scatterers and their high cellular number density. It is experimentally shown that the total, coherent and diffuse signal powers are determined by a structural parameter of the spectral Structure Factor Size and Attenuation Estimator describing the structure factor. Moreover, a two-way repeated measures ANOVA test showed that attenuation (p-value of 0.077) and attenuation compensation (p-value of 0.527) had no significant effect on the diffuse to total power ratio. These results constitute a further step in understanding the physical meaning of first-order statistics of ultrasound images and their relations to QUS techniques. The proposed unifying concepts should be applicable to other biological tissues than blood considering that the structure factor can theoretically model any spatial distribution of scatterers.**

***Index Terms*—Quantitative ultrasound (QUS), Tissue characterization, Erythrocyte aggregation, Homodyned K-distribution, Structure Factor Size and Attenuation Estimator (SFSAE), Backscatter coefficient (BSC).**

I. Introduction

This work was financially supported by the Canadian Institutes of Health Research (grant #MOP–84358). This work has also been carried out in the framework of the Labex MEC (ANR-10-LABX-0092) and of the A*MIDEX project (ANR-11-IDEX-001-02), funded by the "Investissements d'Avenir" French Government program managed by the French National Research Agency (ANR). The authors are grateful to the anonymous reviewers for their helpful comments.

F. Destrempes is with the Laboratory of Biorheology and Medical Ultrasonics, University of Montreal Hospital Research Center (CRCHUM), Montréal, H2X-0A9, Canada.

E. Franceschini is with the Laboratoire de Mécanique et d'Acoustique LMA, CNRS, UPR 7051, Aix-Marseille University, Centrale Marseille, F-13402 Marseille Cedex 20, France.

F. T. H. Yu is with the Center for Ultrasound Molecular Imaging and Therapeutics, University of Pittsburgh, Pittsburgh, PA 15213, USA.

G. Cloutier is with the Laboratory of Biorheology and Medical Ultrasonics, University of Montreal Hospital Research Center (CRCHUM), Montréal, H2X-0A9, Canada, with the Department of Radiology, Radio-Oncology and Nuclear Medicine, University of Montreal, Montréal, H3T-1J4, Canada, and with the Institute of Biomedical Engineering, University of Montreal, Montréal, H3T-1J4, Canada.

Two quantitative ultrasound (QUS) backscatter approaches for determining tissue microstructures from radiofrequency (RF) echoes have received broad interest for the past 30 years: 1) first-order statistical properties of the echo envelope of RF signals; and 2) fitting the spectrum of backscattered RF echoes to an estimated spectrum by an appropriate theoretical scattering model. Whereas spectral QUS approaches propose quantitative measures that are usually closely related to tissue properties, they require estimating the instrumentation spectrum through a reference measurement. Statistical QUS approaches do not have this requirement, but the relation between statistical parameters and tissue properties needs further deepening. Thus, it is of interest to understand the explicit relation between statistical echo envelope parameters and spectral approaches. Notably, one would like to know how much information is lost by considering the echo envelope rather than RF signals, which contain the phase information.

The statistical approach based on the echo envelope has been studied in the context of breast tumor classification [1]–[6], cardiac tissue characterization [7]–[9], atherosclerotic plaque characterization [10]–[12], liver fibrosis [13], and detection of landmarks in fetal brain [14]. Under this approach, statistical parameters are used as features for tissue characterization. Among statistical models for the echo envelope, the homodyned K-distribution [15], [16] has been used in statistical QUS in [4], [5], [9]. Among other models that were also used in this context, let us mention the Nakagami distribution [2]–[4], [6], [7], [14], which is an approximation of the homodyned K-distribution [17, Section 10.3.4], and the K-distribution [1], [8], which is a special case of the homodyned K-distribution. The homodyned K-distribution covers the case of dense or sparse scatterers, whether correlated or not, [16]. The Nakagami distribution considers the same scatterers' configurations [18], but the two shape parameters of the homodyned K-distribution are intertwined into a single Nakagami parameter [19]. The K-distribution assumes a vanishing coherent component, and hence, does not cover the case of strongly organized scatterers [20]. Mixtures of distributions have also been studied in the context of QUS based on the following statistical models: the Rayleigh distribution [10], [13], which corresponds to the special case of fully developed speckle and the gamma distribution [11], used for interpolated B-mode data. See [17], [19] for additional echo envelope distributions and references.

The most frequently used theoretical scattering model under the spectral approach is the spherical Gaussian model developed by Lizzi *et al.* [21], [22] and describing the tissue as a random inhomogeneous continuum with impedance

This article has been accepted for publication in a future issue of this journal, but has not been fully edited. Content may change prior to final publication. Citation information: DOI 10.1109/TMI.2015.2479455, IEEE Transactions on Medical Imaging

fluctuations. The spherical Gaussian model yields two tissue properties: the average scatterer size and the acoustic concentration (*i.e.*, the product of the scatterer number density by the square of the relative impedance difference between scatterers and the surrounding medium). This approach has been used to assess the response to therapy [23] and to differentiate between diseased and healthy tissues or to detect cancer tumors, for the eye [24], the prostate [25], the breast [26], [27], and cancerous lymph nodes [28]. When using this classical scattering model, scatterers are assumed to be independently and randomly distributed (*i.e.*, to have a low scatterer concentration). However, the assumption of randomly distributed scatterers may not hold in concentrated media such as blood and tumors with densely packed cells [29]–[31]. A model adapted to concentrated media is the Structure Factor Model (SFM) used in blood characterization [32], [33]. The SFM is based on the assumption that at high scatterer concentrations, interference effects are mainly caused by correlations between the spatial positions of individual scatterers, *i.e.*, caused by coherent scattering. The SFM sums the contributions from individual cells and models the cellular interaction by a statistical mechanics structure factor, which is defined as the Fourier transform of the spatial distribution of cells [32], [33]. Experiments on tissue-mimicking phantoms [34] and on concentrated cell pellet biophantoms [35], [36] showed that the SFM was more suitable than other classical scattering models (such as the spherical Gaussian model) for dealing with concentrated media.

In this paper, the first aim was to integrate the structure factor, previously used to describe the backscatter coefficient (BSC), into a physical interpretation of statistical parameters of an echo envelope model. For this purpose, we considered the uncompressed and unfiltered echo envelope of RF signals obtained from ultrasound echography of biological tissues. Namely, the echo envelope was viewed as the modulus of the complex analytic signal obtained from the RF signals based on Hilbert transform. The echo envelope can also be viewed as the modulus of the demodulated in-phase and quadrature (IQ) complex signal, obtained after demodulation around the transducer's center frequency. In the proposed approach, scatterers forming the underlying tissue were viewed as randomly positioned, thus forming a random process. Hence, the amplitude of the echo envelope was considered as a random variable and so was the demodulated IQ signal. A mixture of homodyned K-distributions (MHK) model was used to describe the echo envelope in a region-of-interest (ROI) of an ultrasound image, together with statistical parameters of this model. MHK statistical parameters were then related to first-order statistics of the echo envelope and of the IQ signal, and physically interpreted by considering the structure factor intervening in the BSC. This yielded explicit relations between MHK statistical parameters, on one hand, and the SFM, on the other hand. Note that IQ signals were considered in the proposed theoretical framework only as a mean of bridging (mathematically) the gap between MHK statistical parameters and spectral BSC parameters.

The second aim of this study was to test the proposed unification of QUS concepts in the context of RBC aggregation. The choice of this example was motivated by the fact that, unlike the assumption made in [20], [37], scatterers' positions cannot be assumed to be independent and uniformly distributed in the scattering volume, due to their aggregation and their high cellular number density, so that the structure factor intervenes. In particular, the diffuse to total signal power ratio introduced later was investigated as a statistical structural parameter related to RBC aggregation, as it was shown to be not significantly affected by attenuation. Finally, based on established relations between MHK statistical parameters and the structure factor, the diffuse to total signal power ratio was related to a spectral parameter (the mean isotropic aggregate diameter) using an approximation of the SFM [38], [39].

II. Mixtures of homodyned K-distributions

In this section, MHK are introduced to model the echo envelope over a region in an ultrasound image.

A. Model

In the presence of a scattering medium filled with monodisperse scatterers, the homodyned K-distribution [15] was proposed as a general model of the echo envelope [16]. The probability density function (PDF) of the homodyned K-distribution can be expressed as [19]

$$P_{\mathrm{HK}}(A \mid \varepsilon, \sigma^2, \alpha) = \int_0^\infty u J_0(u\varepsilon) A J_0(uA) \big(1 + \frac{u^2\,\sigma^2}{2}\big)^{-\alpha}\, du \tag{1}$$

where A is the echo envelope (*i.e.*, the modulus of the complex IQ signal), $\varepsilon \geq 0$, $\sigma^2 > 0$, $\alpha > 0$, and J_0 denotes the Bessel function of the first kind of order 0. The parameter α is called the scatterer clustering parameter, and ε^2 and $2\sigma^2\alpha$ are the coherent and diffuse signal powers, respectively. The parameter $\mu = \varepsilon^2 + 2\sigma^2\alpha$ is the total signal power[1].

Given an ROI in an ultrasound image of soft tissues, various scatterer kinds (differing in size, spatial distribution and acoustical contrast) might be present, and to each kind might correspond one (or a few) homodyned K-distributions, depending on the variability of the coherent component ε, the mean intensity μ, or the clustering parameter α. Thus, to cover the general case, we propose as model for the echo envelope A, finite mixtures of homodyned K-distributions:

$$P(A) \approx \sum_{j=1}^{\ell} p_j P_{\mathrm{HK}}(A \mid \varepsilon_j, \sigma_j^2, \alpha_j). \tag{2}$$

Note that the special case of a single distribution is contained in the proposed model, upon taking the proportions $p_1 = 1$ and $p_j = 0$ for $j \neq 1$.

B. ROI segmentation and estimation of parameters

To estimate parameters of the mixture model of homodyned K-distributions in an ROI, pixels of the ROI were classified into ℓ regions according to a segmentation algorithm based

[1]Note that in [16], the PDF of the homodyned K-distribution was expressed in terms of the parameters ε, $\tau^2 = \sigma^2\alpha$ and α (denoted "s", "σ^2", and "μ" in that reference).

This article has been accepted for publication in a future issue of this journal, but has not been fully edited. Content may change prior to final publication. Citation information: DOI 10.1109/TMI.2015.2479455, IEEE Transactions on Medical Imaging

TABLE I
STATISTICAL PARAMETERS OF THE ECHO ENVELOPE, THEIR RELATION WITH STATISTICS OF THE IQ SIGNAL, AND THEIR PHYSICAL INTERPRETATION IN TERMS OF THE BSC (IF ANY)

Notion	Notation	Statistical parameters of the echo envelope	Statistics of the IQ signal	Physical interpretation
Echo envelope amplitude	A		$\lvert IQ\rvert$	
Echo envelope intensity	$I = A^2$		$\lvert IQ\rvert^2$	
Total signal power	μ	$\sum_{j=1}^{\ell} p_j \mu_j$	$E[\lvert IQ\rvert^2]$	$\pi c_0 \int_0^\infty \lvert\mathcal{H}(\omega)\rvert^2 \mathcal{D}(z_0,k) BSC(k)\, d\omega$
Coherent signal power	ε^2	$\sum_{j=1}^{\ell} p_j \varepsilon_j^2$	$E[\lvert E_{\text{loc},z}[IQ]\rvert^2]$	$\pi c_0 \int_0^\infty \lvert\mathcal{H}(\omega)\rvert^2 \mathcal{D}(z_0,k)$ $\operatorname{sinc}^2((k-k_c)\ell_z) BSC(k)\, d\omega$
Diffuse signal power	$\mu - \varepsilon^2$	$\sum_{j=1}^{\ell} p_j 2\sigma_j^2 \alpha_j$	$E[Var_{\text{loc},z}[IQ]]$	$\pi c_0 \int_0^\infty \lvert\mathcal{H}(\omega)\rvert^2 \mathcal{D}(z_0,k)$ $\left(1 - \operatorname{sinc}^2((k-k_c)\ell_z)\right) BSC(k)\, d\omega$
Diffuse to total signal power ratio	$\frac{1}{\kappa+1}$	$\frac{\mu-\varepsilon^2}{\mu}$	$\frac{E[Var_{\text{loc},z}[IQ]]}{E[\lvert IQ\rvert^2]}$	$\frac{\int_0^\infty \lvert\mathcal{H}(\omega)\rvert^2 \mathcal{D}(z_0,k)\left(1-\operatorname{sinc}^2((k-k_c)\ell_z)\right) BSC(k)\, d\omega}{\int_0^\infty \lvert\mathcal{H}(\omega)\rvert^2 \mathcal{D}(z_0,k) BSC(k)\, d\omega}$

on a Markov random field (MRF) model. This segmentation algorithm is presented in Appendix A. Next, conditional to the ROI segmentation, the amplitude of the echo envelope on each region $j = 1, ..., \ell$ was modeled by a homodyned K-distribution $P_{\text{HK}}(A \mid \varepsilon_j, \sigma_j^2, \alpha_j)$ as in Eq. (1). Homodyned K-distribution parameters were estimated on each region with the method presented in [40].

Then, based on the MHK model, the following statistical parameters were considered (total and coherent signal powers):

$$\mu = \sum_{j=1}^{\ell} p_j(\varepsilon_j^2 + 2\sigma_j^2\alpha_j); \quad \varepsilon^2 = \sum_{j=1}^{\ell} p_j \varepsilon_j^2. \tag{3}$$

In this study, the diffuse to total signal power ratio was also considered:

$$1/(\kappa+1) = (\mu - \varepsilon^2)/\mu, \tag{4}$$

where κ is the structure parameter $\varepsilon^2/(\mu - \varepsilon^2)$ of [40].

In Appendix B, it is shown that the MHK model is identifiable; *i.e.*, two such mixtures yielding the same PDF must have the same parameters (up to permutation of the indices j in Eq. (2)). The identifiability problem is important for the following reasons. Firstly, the estimation of finite mixtures of distributions belonging to a given family of distributions does not make sense unless the model is identifiable, for otherwise there would not be a unique solution. Secondly, in the context of ultrasound image segmentation (as in [41]) and statistical tissue characterization (as in [11]), the identifiability of a finite mixture model means that the distributions corresponding to each biological tissue layer appearing in an ROI can be retrieved from an estimation of the mixture model in that ROI. From the identifiability property of the proposed model, it follows that the expressions of statistical parameters introduced in Eqs. (3) and (4) are unambiguous.

III. RELATION BETWEEN MHK STATISTICAL PARAMETERS AND FIRST-ORDER STATISTICS OF THE ECHO ENVELOPE AND OF THE DEMODULATED ANALYTIC SIGNAL

MHK statistical parameters introduced in Section II-B are related to two statistics of the echo envelope and of the IQ signal: 1) $E[I]$, where E denotes averaging and I is the intensity (*i.e.*, the square of the echo envelope amplitude); and 2) $E[\lvert E_{\text{loc},z}[IQ]\rvert^2]$, where $E_{\text{loc},z}$ denotes local averaging along the axial direction on an interval of length equal to the axial resolution length. Note that the intensity corresponds to the squared modulus of the IQ signal. To derive the relations below, discretization of a continuous scattering model has been considered, as in [19].

A. Case of a single homodyned K-distribution

In [16], it was proposed to view the IQ signal as a random walk (in the complex plane) equivalent to a sum of random phasors, with bias $\vec{\varepsilon}$ whose modulus squared is equal to the parameter ε^2 of the homodyned K-distribution modeling the corresponding echo envelope. Now, as will be seen in Section IV-C, if scatterers are not spatially organized independently and uniformly, then the interpretation of scatterers as independent random phasors might not hold. For this reason, we consider a continuous interpretation of the scattering medium [42], [43], rather than a discrete one (*i.e.*, based on finitely many scatterers). More precisely, this model can be viewed as a discretization of a continuous scattering model, in which phasors are viewed as local fluctuations in density and compressibility describing the continuous medium. Under this interpretation, there are several more phasors than scatterers, and they correspond to local fluctuations clustered inside and outside scatterers.

So, we consider, as in [19], a stochastic process of the form

$$\mathbf{A}_N = \vec{\varepsilon} + \frac{1}{N^{1/2}} \sum_{n=1}^{N} \mathbf{a}_n, \tag{5}$$

This article has been accepted for publication in a future issue of this journal, but has not been fully edited. Content may change prior to final publication. Citation information: DOI 10.1109/TMI.2015.2479455, IEEE Transactions on Medical Imaging

where $\vec{\varepsilon}$ is a vector in the complex plane and random complex variables $\mathbf{a}_n$ (*i.e.*, phasors corresponding to local fluctuations in density and compressibility) are identically and independently distributed, each phasor having a random amplitude independent of its uniformly distributed phase. The quantity $\overline{N}$ represents the average value of the variable number N of phasors (within one resolution cell). Then, we model the IQ signal on an interval of a scan line of length equal to one resolution cell as the limit process $\lim_{\overline{N}\to\infty} \mathbf{A}_N$. Under this point of view, the bias $\vec{\varepsilon}$ is interpreted as $E_{\text{loc},z}[IQ]$. The modulus A of this asymptotic process is then viewed as the echo envelope on this interval of the scan line. As presented in [19], its PDF is a homodyned K-distribution with parameters $\varepsilon = |\vec{\varepsilon}|$, $\sigma^2 = \langle|\mathbf{a}_n|^2\rangle/(2\alpha)$, and α, as follows from Jakeman and Tough generalization of the Central Limit Theorem, assuming that N is distributed according to a negative binomial distribution with variance equal to $\overline{N}^2\big(1/\overline{N}+1/\alpha\big)$. The consideration of negative binomial distributions is quite general since from [44], the distribution on the number of points in an arbitrary (*possibly inhomogeneous*) Poisson process can be approximated by a mixture of such distributions.

Then, assuming that the bias $\vec{\varepsilon}$ has squared modulus concentrated around its mean value (but with possibly varying phase) as one varies the position of scan lines and the location of intervals (of length one resolution cell), one obtains a homodyned K-distribution with same parameters, with the interpretation $\varepsilon^2 = E[|E_{\text{loc},z}[IQ]|^2]$. Moreover, the mean intensity $E[I]$ under the homodyned K-distribution is equal to the parameter $\mu = \varepsilon^2 + 2\sigma^2\alpha$ [19, Table 3].

B. Case of mixtures of homodyned K-distributions

In the general case of MHK, one deduces from the previous section, upon taking weighted sums of statistics corresponding to each distribution, that the statistics μ (the total signal power) and ε^2 (the coherent signal power) of Eq. (3) correspond to $E[I]$ and $E[|E_{\text{loc},z}(IQ)|^2]$ on the ROI. Therefore, the diffuse signal power $\mu - \varepsilon^2$ corresponds to $E[Var_{\text{loc},z}[IQ]]$, where Var denotes the variance of a complex variable. Indeed, the average value of the intensity can be viewed as $E[E_{\text{loc},z}[|IQ|^2]]$. Altogether, one obtains:

$$\begin{aligned} &E[I] = \mu; \qquad E[|E_{\text{loc},z}[IQ]|^2] = \varepsilon^2; \\ &E[Var_{\text{loc},z}[IQ]] = \mu - \varepsilon^2. \end{aligned} \tag{6}$$

Therefore, the ratio of the diffuse to total signal power admits the following interpretation

$$E[Var_{\text{loc},z}[IQ]]/E[I] = 1/(\kappa+1). \tag{7}$$

IV. Physical interpretation of first-order statistics of the echo envelope and of the demodulated analytic signal

The various statistics introduced in Section III are now interpreted based on acoustical physics. We consider a single-element focused transducer operating in pulse-echo mode and a scattering volume $\mathbf{V}$ located in the focal zone of the transducer. Underlying hypotheses are: far field regime (the observation distance – the transducer's focal length – is large compared to the size of the volume occupied by scatterers), incident plane wave in the focal zone, weak scattering and Born's approximation. To study statistics of the echo envelope and of the IQ signal, it is convenient to view the operator E of Section III as an average over space and realizations of underlying tissues, per unit volume.

A. Equations of the echo envelope and of the IQ signal

Let ρ_0 and κ_0 be the density and compressibility of the surrounding medium, and ρ and κ be the density and compressibility of the acoustic inhomogeneities. We consider the function

$$\gamma(\mathbf{r}') = \gamma_\kappa(\mathbf{r}') - \gamma_\rho(\mathbf{r}'), \tag{8}$$

where $\mathbf{r}'$ represents the position (x', y', z') in the three-dimensional space (with origin located at the center of the focal zone), $\gamma_\rho(\mathbf{r}') = (\rho(\mathbf{r}') - \rho_0)/\rho(\mathbf{r}')$ and $\gamma_\kappa(\mathbf{r}') = (\kappa(\mathbf{r}') - \kappa_0)/\kappa_0$ are the fractional variations in medium density and compressibility, respectively.

Having considered a single-element focused transducer, it is convenient to define the modulated backscattered amplitude Φ_s as follows:

$$\Phi_s(\mathbf{r}_0, k) = k^2 \int_{\mathbf{V}} \gamma(\mathbf{r}') A_{\text{RI}}^2(\mathbf{r}_0, \mathbf{r}', k) d^3\mathbf{r}', \tag{9}$$

where $\mathbf{r}_0 = (x_0, y_0, z_0)$ is the location of the center of the transducer surface, $k = \omega/c_0$ is the wave number expressed in terms of the angular frequency ω and the speed of sound in the ambient medium c_0, and where $A_{\text{RI}}(\mathbf{r}_0, \mathbf{r}', k)$ denotes the Rayleigh integral of the Green's function over the radiating transducer surface. This notion is defined as

$$A_{\text{RI}}(\mathbf{r}_0, \mathbf{r}', k) = \frac{1}{2\pi} \int \frac{e^{ik|\mathbf{r}_0 + \mathbf{r}_s - \mathbf{r}'|}}{|\mathbf{r}_0 + \mathbf{r}_s - \mathbf{r}'|} d^2\mathbf{r}_s, \tag{10}$$

where $\mathbf{r}_s$ denotes the vector from the transducer's surface center to an arbitrary point of the surface.

Then, based on [45] and taking attenuation into consideration, the RF backscattered signal at time t can be expressed as

$$\begin{aligned} &RF(\mathbf{r}_0, t) \\ &\approx \frac{1}{2} i\rho_0 c_0 \int_{-\infty}^{\infty} k\mathcal{A}^{1/2}(\omega) T(\omega) U(\omega) \Phi_s(\mathbf{r}_0, k) e^{-i\omega t}\, d\omega, \end{aligned} \tag{11}$$

where $i = \sqrt{-1}$, $\mathcal{A}(\omega)$ is the attenuation term of the scattering medium, $T(\omega)$ is the acoustoelectric transfer function of the transducer element, and $U(\omega)$ is the component of the speed of the radiating transducer surface at angular frequency ω.

After application of a bandpass filter $B(\omega)$ on the RF signal, one obtains the analytic signal, which is related to the Hilbert transform of the RF signal, by setting all negative frequency components to 0 and multiplying the other ones by 2. Then, demodulation around the center frequency $f_c = \omega_c/(2\pi)$ yields the IQ signal expressed as:

$$IQ(\mathbf{r}_0, t) \approx \int_0^{\infty} \mathcal{H}(\omega) \Phi_s(\mathbf{r}_0, k) e^{-i(\omega - \omega_c)t}\, d\omega, \tag{12}$$

This article has been accepted for publication in a future issue of this journal, but has not been fully edited. Content may change prior to final publication. Citation information: DOI 10.1109/TMI.2015.2479455, IEEE Transactions on Medical Imaging

where the function $\mathcal{H}(\omega)$ is defined as:

$$\mathcal{H}(\omega) = i\rho_0 c_0 k \mathcal{A}^{1/2}(\omega) B(\omega) T(\omega) U(\omega). \quad (13)$$

Finally, the amplitude of the echo envelope is viewed as the norm of the IQ signal (or equivalently, the analytic signal).

B. Low order moments of the echo envelope and of the IQ signal

To compute average values per unit volume of ultrasound signals over space and realizations of underlying tissues, the single-element transducer is assumed to move parallel to the (x, y) plane to obtain several scan lines (a B-mode image), which correspond to several scatterer realizations. The average over realizations of scatterers corresponds to ensemble averaging $\langle\cdot\rangle$. For a fixed transducer position $\mathbf{r}_0 = (x_0, y_0, z_0)$, we denote (x_0, y_0, z) all points located on the scan line, where z is small (within ± 7 times the resolution length for reported results) compared to the focal length.

First of all, the average $E[I]$ over space of the intensity is the total signal power

$$(c_0/2)\langle \iiint |IQ(\mathbf{r}_0, t)|^2 \, dt \, dx_0 \, dy_0 \rangle \quad (14)$$

scattered per unit volume, where we have used the change of variable $z = (c_0/2)t$. Using Parseval's Theorem applied to the variable t, we thus obtain

$$E[I] = V^{-1}\pi c_0 \int_0^\infty |\mathcal{H}(\omega)|^2 \langle \iint |\Phi_s(\mathbf{r}_0, k)|^2 \, dx_0 \, dy_0 \rangle \, d\omega$$
$$\approx \pi c_0 \int_0^\infty |\mathcal{H}(\omega)|^2 \mathcal{D}(z_0, k) BSC(k) \, d\omega, \quad (15)$$

where V is the volume of $\mathbf{V}$, $\mathcal{D}(z_0, k)$ is the diffraction compensation coefficient and $BSC(k)$ denotes the backscatter coefficient. This important notion in QUS is defined as:

$$BSC(k) = \frac{k^4}{16\pi^2 V} \langle | \int_{\mathbf{V}} \gamma(\mathbf{r}') e^{2ik\mathbf{n}_0 \cdot \mathbf{r}'} \, d^3\mathbf{r}' |^2 \rangle, \quad (16)$$

where $\mathbf{n}_0 = (0, 0, 1)$ is the direction of the incident pressure wave in the focal zone. Arguing as in [46], the diffraction compensation coefficient $\mathcal{D}(z_0, k)$ can be estimated as

$$16\pi^2 \iint |A_{\mathrm{RI}}((0, 0, z_0), (x', y', 0), k)|^4 \, dx' \, dy'. \quad (17)$$

Secondly, we consider the average contribution of the IQ signal along the axial axis through a point (x_0, y_0, z) of the 3D volume on a distance ℓ_z corresponding to the axial resolution:

$$E_{\mathrm{loc},z}[IQ] = \ell_z^{-1} \int_{z-\ell_z/2}^{z+\ell_z/2} IQ(\mathbf{r}_0, \tilde{t} = 2\tilde{z}/c_0) \, d\tilde{z} =$$
$$\int_0^\infty \mathcal{H}(\omega) \Phi_s(\mathbf{r}_0, k) \mathrm{sinc}((k - k_c)\ell_z) e^{-2i(\omega - \omega_c)t} d\omega, \quad (18)$$

where sinc denotes the function $\sin(x)/x$, having used Eq. (12) for the second equality. One then obtains from Parseval's Theorem the following approximation:

$$E[|E_{\mathrm{loc},z}[IQ]|^2] \approx \pi c_0 \times$$
$$\int_0^\infty |\mathcal{H}(\omega)|^2 \mathcal{D}(z_0, k) \mathrm{sinc}^2((k - k_c)\ell_z) BSC(k) \, d\omega. \quad (19)$$

Eqs (15) and (19) express direct relations between the BSC and the statistics $E[I]$ and $E[|E_{\mathrm{loc},z}[IQ]|^2]$ of the echo envelope and of the IQ signal, respectively, under the considered hypotheses, in terms of the instrumentation setting (through factors $T(\omega)B(\omega)U(\omega)$ in Eq. (13) and $\mathcal{D}(z_0, k)$ of Eq. (17)), and tissue attenuation (from the factor $\mathcal{A}^{1/2}(\omega)$ in Eq. (13)). Note that the difference between Eqs (15) and (19) can be interpreted as $E[Var_{\mathrm{loc},z}[IQ]]$. Note also that considering the ratio of these two equations might reduce the effect of the instrumentation and attenuation on each of them.

Thus, based on Eq. (6), the total and coherent signal powers of Eq. (3) can be interpreted with Eqs (15) and (19), respectively. From there, one obtains also the physical interpretation of the diffuse signal power on the ROI as stated in Table I, and hence of the diffuse to total signal power ratio.

C. Introduction of the structure factor

Let us now assume N_s identical scatterers (spatially correlated or not) within the scattering volume $\mathbf{V}$, in addition to the hypotheses considered so far. Then, the BSC can be expressed in the following form under the SFM (see [38])

$$BSC(k) \approx m\sigma_b(k) S(k), \quad (20)$$

where m is the number density of scatterers $\langle N_s \rangle / V$, $\sigma_b(k)$ is the differential backscattering cross-section that depends on acoustic and geometric properties of a single scatterer, and $S(k)$ is the structure factor that depends on the spatial organization of scatterers. The latter quantity is defined as the ensemble average

$$S(k) = \langle \frac{1}{N_s} | \sum_{n=1}^{N_s} e^{2ik\mathbf{n}_0 \cdot \mathbf{r}_n} |^2 \rangle, \quad (21)$$

where $\mathbf{r}_n$ is the position of the nth scatterer, and can be expressed with the so-called pair-correlation function (see [38]), which is related to the distribution of distances between pairs of scatterers.

Substituting Eq. (20) into Eq. (15) reveals that the mean intensity depends not only on the number of scatterers, but also on their spatial organization through the structure factor $S(k)$. In fact, one may not assume that $E[I]$ is proportional to the number of scatterers within the scattering volume, unless $S(k)$ is a constant, which implies that $S(k) = 1$ [47]. This latter condition (*i.e.*, $S(k) = 1$) means that scatterers are randomly distributed according to a homogeneous Poisson process [48] (*i.e.*, independently and uniformly distributed), which implies that scatterers are small and sparse compared to the scattering volume. From this observation, it follows that the model [20], [37] expressing the complex IQ signal as a sum of independent random phasors, *each phasor corresponding to one scatterer*, does not hold unless scatterers are distributed according to a homogeneous Poisson process. On the other hand, Eqs (15) and (19) take into account a general model for the scatterers' spatial organization.

Thus, combining Sections II, III and IV, relations between MHK statistical parameters and the structure factor intervening in the BSC were reached under the considered hypotheses.

This article has been accepted for publication in a future issue of this journal, but has not been fully edited. Content may change prior to final publication. Citation information: DOI 10.1109/TMI.2015.2479455, IEEE Transactions on Medical Imaging

D. A special case: the SFSAE model

Principles stated above are now developed in the context of a BSC parametric spectral method considering aggregated cells in a dense medium, such as aggregated red blood cells in blood. In the context of ultrasound blood characterization based on spectral methods, the inverse problem approach (*i.e.*, fitting approach) has been performed using the Structure Factor Size and Attenuation Estimator (SFSAE) model described in [38]. The SFSAE model uses the second-order Taylor development of the structure factor S:

$$S(k) \approx W - \frac{12}{5} a^2 D^2 k^2, \tag{22}$$

where $W = \lim_{k\to 0} S(k)$ is the so-called packing factor, a is the RBC radius and D is the mean isotropic aggregate diameter (derived from the mean gyration radius) normalized by the RBC diameter (equivalently, D is the mean isotropic aggregate radius normalized by the RBC radius). From [39], W can be expressed as a quadratic function of D, reducing the BSC parametrization to one parameter. Therefore, combining Eqs (6), (15), (20) and (22), the statistical parameter μ of Eq. (3) can be expressed as a quadratic function of D. A similar relation can be derived for the coherent signal power ε^2, based on Eqs (6), (19), (20) and (22), and hence also for the diffuse signal power $\mu - \varepsilon^2$.

Therefore, one concludes that there are relations of the form

$$\begin{aligned} &\mu - \varepsilon^2 = b' + c'D + d'D^2; \quad \mu = b + cD + dD^2, \\ &\frac{1}{(\kappa+1)} = \frac{\mu - \varepsilon^2}{\mu} \approx \frac{b' + c'D + d'D^2}{b + cD + dD^2}, \end{aligned} \tag{23}$$

where the six coefficients b', c', d', b, c, and d are real numbers that do not depend on D, but only on the instrumentation, scattering properties of one RBC, the hematocrit and ultrasound (US) attenuation [2]. In this manner, the statistical MHK parameter $1/(\kappa+1)$ is related to the spectral SFSAE parameter D.

V. Experimental data: Application to blood scattering

Sequences of US images were obtained from experiments described in Sections III-A and III-B.1 of reference [38]. These experiments are briefly summarized in this section.

US measurements were performed in a Couette flow device to produce a linear blood velocity gradient (*i.e.*, shear rate) at a given rotational speed. The system consisted of a rotating inner cylinder surrounded by a fixed concentric cylinder with respective diameters of 160 and 164 mm. A 60 ml porcine blood sample (having a hematocrit of 40%) was sheared in the 2 mm annular space between both coaxial cylinders. A Vevo 770 high-frequency ultrasound system (Visualsonics Inc., Fujifilm, Toronto, Canada) with an oscillating single-element 25-MHz focused transducer (focal depth of 15 mm, aperture diameter of 7.1 mm, axial resolution of 0.070 mm, lateral resolution of 0.140 mm) was used to collect RF backscatter signals from blood. RF data were acquired at a sampling frequency of 250 MHz with 8 bit resolution. The probe was mounted in the side wall of the fixed outer cylinder and was positioned to have its focal zone at the center of the gap between both cylinders. To ensure ultrasonic coupling, the hole within the outer stationary cylinder (containing the probe) was filled with an agar gel based mixture fitting the circular geometry in contact with blood. The agar gel contained a specific concentration of 50 μm cellulose scattering particles (S5504 Sigmacell, Sigma Chemical, Saint-Louis, MO) to control the attenuation coefficient. Five experiments were performed with five mixtures having Sigma Cell (SC) concentrations varying from 0% to 1% (w/w). The 0% concentration constituted the non-attenuating gel and the four other mixtures mimicked skin attenuation.

In this study, 0.25%, 0.5%, 0.75%, 1% SC were used to assess the robustness of the QUS statistical characterization method to attenuation. The BSC spectral characterization included an attenuation compensation, as described in Eq. (1) of [38]. See also Section VI below for the parametrization of the BSC with the SFSAE model.

Prior to each measurement, the blood was sheared at 200 s^{-1} during 30 s to disrupt RBC aggregates. The shear rate was then reduced to residual values of 5, 10, 20, 30, and 50 s^{-1} for 90 s until an equilibrium in the state of aggregation was reached. For each shear rate, 5 B-mode images were successively constructed from acquired RF echoes each 16 s for a total period of analysis of 80 s. For 180 vertical lines at the center of B-mode images, echoes were selected within a rectangular window of axial length 1 mm, which yielded an ROI of 2.8×1.0 mm^2 (180×318 pixels^2). This protocol was repeated five times with the same blood and with each of the five agar-based attenuating phantoms.

The attenuation model adopted in [38] and introduced in Eq. (11) is based on the attenuation function given by

$$\mathcal{A}(k) = e^{-4\alpha_0 k/8.68(c/2\pi)} = e^{-4\alpha_0 f/8.68}, \tag{24}$$

where k is the wavenumber, c is the mean speed of sound in the intervening tissue layers, f is the frequency in MHz, and α_0 is the attenuation coefficient (in dB/MHz). Note that, in this equation, the factor 4 comes from consideration of the attenuation factor for the power spectrum of the RF signals. In the case of the Couette experimental design, one has $\alpha_0 = \alpha_{\text{blood}} e_{\text{blood}} + \alpha_{\text{SC}} e_{\text{SC}}$, where α_{blood} and α_{SC} are attenuation coefficients of blood and skin-mimicking phantoms, respectively. Variables e_{blood} and e_{SC} correspond to thicknesses of corresponding tissue layers. Average values of attenuation coefficients α_{blood} and α_{SC} are reported in Section III-B.3 and Table I, respectively, of [38].

VI. Experimental results

Concepts presented in Sections II, III and IV are now illustrated in the context of RBC aggregation. Thus, 1) the mixture of $\ell \leq 3$ homodyned K-distributions was evaluated to characterize five RBC aggregation levels obtained in a Couette flow device for five attenuation skin-mimicking phantoms. In particular, the robustness of the diffuse to total signal power

[2]Note that parameter $1/(\kappa+1)$ is a function of 5 unknowns after normalization of any of the 6 coefficients appearing in Eq. (23).

This article has been accepted for publication in a future issue of this journal, but has not been fully edited. Content may change prior to final publication. Citation information: DOI 10.1109/TMI.2015.2479455, IEEE Transactions on Medical Imaging

TABLE II
PROPORTIONS (p_j) AND MEAN INTENSITIES (μ_j) OF EACH SEGMENTED REGION IN FIRST FRAMES OF DATA ACQUIRED WITHOUT ATTENUATION, ACCORDING TO FIVE SHEAR RATES. SEE FIG. 1 AND TABLE I.

Shear rates (s^{-1})	p_1	μ_1	p_2	μ_2	p_3	μ_3
5	0.53	1.0	0.17	1.7	0.30	4.7
10	0.66	0.85	0.21	4.4	0.13	4.4
20	0.86	0.60	0.11	3.6	0.03	3.6
30	0.87	0.22	0.08	1.1	0.05	1.1
50	0.96	0.072	0.04	0.42	0	NA

ratio $1/(\kappa+1)$ of the MHK model was tested. 2) The statistic $E[|E_{\text{loc},z}[IQ]|^2]$ was compared with the MHK parameter ε^2 to investigate whether this interpretation is empirically valid. 3) Lastly, the diffuse to total signal power ratio was related to the SFSAE spectral parameter D describing erythrocyte clustering using a nonlinear fitting model.

A. Mixtures of homodyned K-distributions

1) ROI segmentation: In the acquired images, regions with different levels of echogenicity were present and it was found that data (gray levels of the echo envelope) within the rectangular ROI could not be assumed to have a unimodal histogram. See Fig. 1, third column, bottom example. Thus, for each image of the sequences acquired as above, pixels of the rectangular ROI were classified into three classes or less based on the segmentation method of Appendix A. The number of classes corresponds to the number ℓ of homodyned K-distributions in the estimated mixture model.

In Fig. 1, second column, the segmentation into three classes or less of the ROI in the first frame corresponding to 0% SC (no attenuation) are presented for shear rates varying from 5 s^{-1} to 50 s^{-1}, using the proposed algorithm. Corresponding proportions and mean intensities on each segmented class are reported in Table II. The other levels of attenuation yielded similar results. As can be seen in this figure and this table, it cannot be assumed that a single homodyned K-distribution suffices to model the echo envelope in an ROI, even more so in the case of a low shear rate (*i.e.*, high aggregation level).

2) Statistical parameters: Given the segmentation of the ROI, the set of amplitudes (*i.e.*, gray levels of the echo envelope) on each non-empty class of pixels $j = 1, 2, 3$ was viewed as an independent identically distributed (i.i.d.) sample of the amplitude. Then, parameters of the homodyned K-distribution (ε_j, σ_j^2 and α_j) on each of these sets, for each image of the sequence, were estimated with the method introduced in [40]. From there, parameters μ and ε^2 for each image were obtained as weighted sums of corresponding parameters on each non-empty class, according to Eq. (3), where ℓ stands for the number of non-empty classes of pixels. Winsorized means [49] of parameters μ, ε^2 and $1/(\kappa+1) = (\mu - \varepsilon^2)/\mu$ over the 5 images of a sequence[3] were computed to yield estimated values of these parameters, for each of the 25 sequences corresponding to 5 shear rates. These values are reported in Table III. As can be seen, values of μ, ε^2 and $1/(\kappa+1)$ depend on shear rate. Moreover, μ and ε^2 also depend on the attenuation. However, $1/(\kappa+1)$ seems to be less affected by attenuation.

To further verify this statement, the estimation of statistical parameters was applied on the same data, but after attenuation compensation, based on attenuation coefficients estimated with the SFSAE method. Then, a two-way repeated measures ANOVA test was performed to evaluate the effect of attenuation (first factor) with or without attenuation compensation (second factor) on the data for the five levels of aggregation. This test indicated that attenuation (p-value of 0.077) and attenuation compensation (p-value of 0.527) had no significant effect on the diffuse to total power ratio. Statistical tests were performed using SigmaStat (Systat Software, San Jose, CA).

B. Physical interpretation of the coherent component

The statistics $E[|E_{\text{loc},z}[IQ]|^2]$ were computed directly on the demodulated signals and compared with the estimated values of $\varepsilon^2 = \sum_{j=1}^{\ell} p_j \varepsilon_j^2$ to assess if this interpretation of ε^2, which is related to Eq. (19), is valid. Figure 2 shows a comparison between these two statistics for various levels of attenuation and aggregation. As can be seen, there is a close match between these two statistics. In these tests, the local average $E_{\text{loc},z}[IQ]$ was computed over a distance of 0.070 mm, which corresponded to the axial length of one resolution cell. The nominal center frequency used for demodulation was computed as the first moment of the power signal spectrum.

Since $E_{\text{loc},z}[IQ]$ is a local average, the identity $\varepsilon^2 \approx E[|E_{\text{loc},z}[IQ]|^2]$ suggests that ε^2 can be retrieved by summing up local estimates. Hence, we have considered local sliding windows of size 0.32×0.16 mm^2 (21×51 pixels^2), corresponding to 2.32 resolution length in each dimension [50], with center position sweeping the ROI with a step of 7 pixels in the axial direction. Moreover, each sliding window was clipped with the specific segmented region (produced by the proposed segmentation method) containing its center. Then, parameters ε_w and μ_w of a single homodyned K-distribution were estimated within each clipped sliding window w. From there, a parametric image could be obtained by displaying at each ROI pixel the statistical parameter $(\mu_w - \varepsilon_w^2)/E[\mu_w]$, where w was centered at this pixel. See Fig. 3 for an illustration of such parametric images. For the color bar, the few pixels in the top image (less than 1%) with value greater than 1.5 were displayed with value 1.5.

Furthermore, for each sequence of images, the Winsorized mean over its frames of the average value $E[(\mu_w - \varepsilon_w^2)]/E[\mu_w]$ (computed on each frame) was compared with $(\mu - \varepsilon^2)/\mu$. A Wilcoxon signed rank test showed that there was no significant difference between these two statistics (p-value of 0.307). Thus, proposed parametric images exemplified in Fig. 3 were closely related to the diffuse to total signal power ratios.

C. Relation between the diffuse to total signal power ratio and the SFSAE model

Assuming the SFSAE model for the BSC, the coefficients appearing in Eq. (23) were estimated with a nonlinear fitting model using Mathematica software (Wolfram Research,

[3]Here, Winsorized means are computed over 5 values as $(2x_2 + x_3 + 2x_4)/5$, where $x_1, x_2, ..., x_5$ are the 5 values labeled in increasing order. This amounts to replacing the lowest value x_1 and highest value x_5 by x_2 and x_4, respectively, to avoid outliers.

This article has been accepted for publication in a future issue of this journal, but has not been fully edited. Content may change prior to final publication. Citation information: DOI 10.1109/TMI.2015.2479455, IEEE Transactions on Medical Imaging

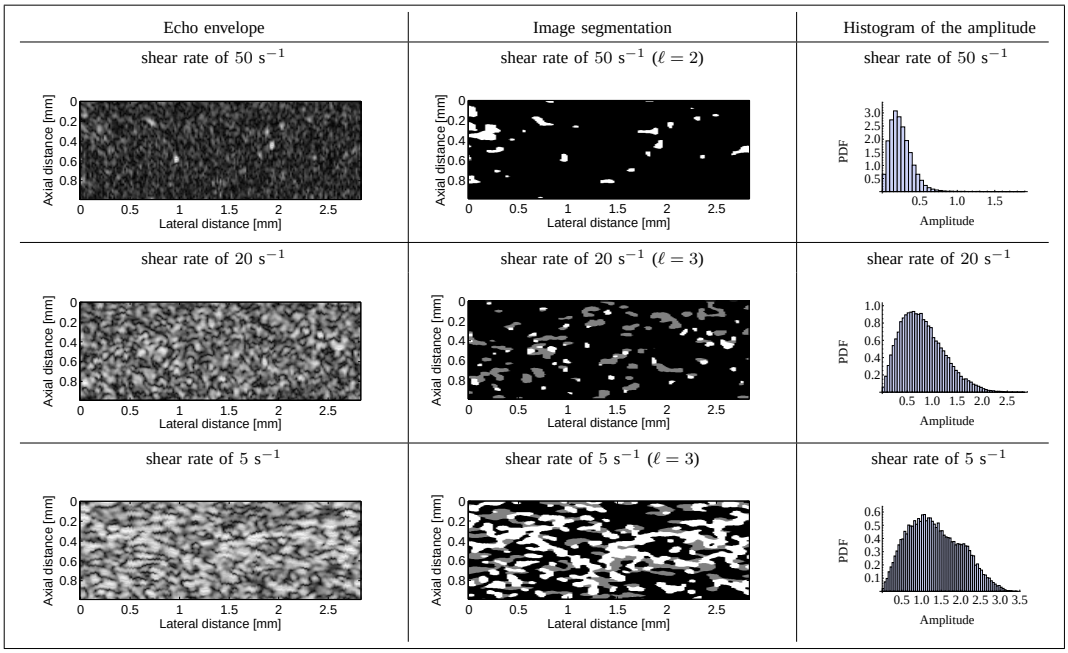

Fig. 1. Examples of segmented ROI into three classes or less according to statistical properties of the amplitude of B-mode images. Left: B-mode images; second column: segmentation into ℓ classes (corresponding to the number of homodyned K-distributions in the mixture model); right: histograms of the amplitude of B-mode images. From top to bottom, shear rates are 50 s^{-1}, 20 s^{-1} and 5 s^{-1}. These examples correspond to 0% SC (no attenuation). Statistical parameters of each class could be retrieved uniquely from the PDF of the echo envelope amplitude in the ROI (identifiability of finite mixtures of homodyned K-distributions).

TABLE III

PARAMETERS μ, ε^2 AND $1/(\kappa+1)$ OBTAINED WITH THE HOMODYNED K-DISTRIBUTION MIXTURE MODEL FOR 5 LEVELS OF ATTENUATION (0%, 0.25%, 0.5%, 0.75%, AND 1% SC) AT 5 SHEAR RATES (5, 10, 20, 30 AND 50 s^{-1}). THE PACKING FACTORS W AND DIAMETERS D OBTAINED WITH THE SFSAE MODEL ARE ALSO INDICATED.

SC (%) attenuation coefficient (dB/MHz)	QUS parameters	5 s^{-1}	10 s^{-1}	20 s^{-1}	30 s^{-1}	50 s^{-1}
0% (0.007 ± 0.0019 dB/MHz)	μ, ε^2 $1/(\kappa+1)$ W, D	2.25, 1.80 0.200 24.56, 10.11	1.54, 1.16 0.248 9.14, 4.59	0.859, 0.542 0.368 3.90, 2.68	0.295, 0.149 0.498 1.39, 1.35	0.00849, 0.0255 0.698 0.44, 0.82
0.25% (0.115 ± 0.024 dB/MHz)	μ, ε^2 $1/(\kappa+1)$ W, D	0.757, 0.569 0.247 36.97, 10.87	0.472, 0.337 0.279 10.14, 5.25	0.274, 0.177 0.353 3.78, 3.28	0.0930, 0.0480 0.470 1.14, 1.49	0.0274, 0.00935 0.673 0.46, 0.89
0.5% (0.219 ± 0.030 dB/MHz)	μ, ε^2 $1/(\kappa+1)$ W, D	0.283, 0.215 0.244 23.33, 9.05	0.157, 0.112 0.268 9.35, 4.83	0.0800, 0.0550 0.319 3.32, 2.85	0.0269, 0.0146 0.460 1.34, 1.25	0.00838, 0.00339 0.596 0.53, 0.98
0.75% (0.320 ± 0.035 dB/MHz)	μ, ε^2 $1/(\kappa+1)$ W, D	0.133, 0.102 0.219 26.83, 11.11	0.0743, 0.0566 0.246 9.08, 4.84	0.0399, 0.0292 0.269 3.07, 3.11	0.0132, 0.00730 0.443 1.36, 1.59	0.00393, 0.00154 0.602 0.38, 0.90
1% (0.411 ± 0.040 dB/MHz)	μ, ε^2 $1/(\kappa+1)$ W, D	0.167, 0.131 0.210 23.01, 11.08	0.107, 0.0800 0.250 10.86, 5.07	0.0530, 0.0387 0.279 3.57, 3.19	0.0146, 0.00955 0.350 1.16, 1.62	0.00460, 0.00171 0.627 0.35, 1.02

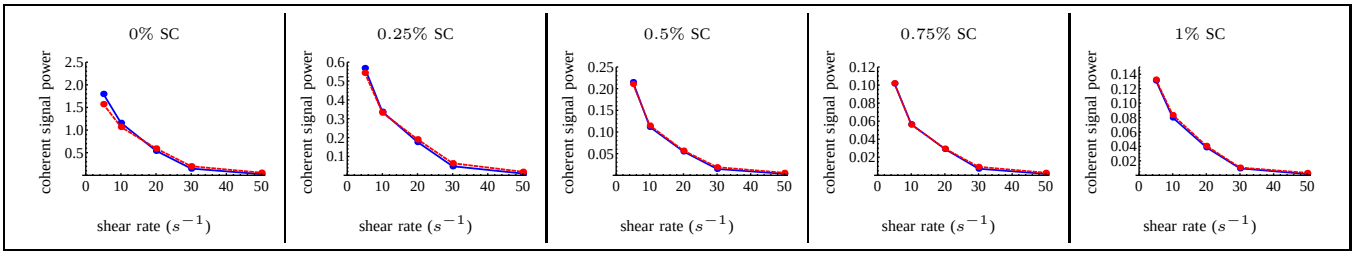

Fig. 2. Curves of ε^2 (—) and $E[|E_{\text{loc},z}[IQ]|^2]$ (—) as a function of the shear rate for five levels of attenuation. The parameter ε^2 can be interpreted as the mean squared modulus of the local average IQ signal along the axial direction.

Champaign, Il) based on values of $1/(\kappa+1)$, μ, and D estimated on the data acquired without attenuation (*c.f.*, first row of Table III), viewed as a training set. The coefficients (in volts^2) were equal to $b' = -0.0469$, $c' = 0.143$,

This article has been accepted for publication in a future issue of this journal, but has not been fully edited. Content may change prior to final publication. Citation information: DOI 10.1109/TMI.2015.2479455, IEEE Transactions on Medical Imaging

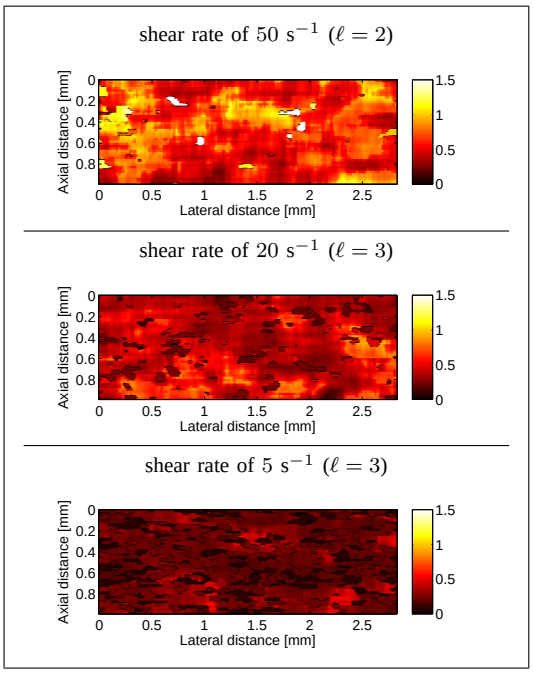

Fig. 3. Examples of diffuse signal power $(\mu_w - \varepsilon_w^2)$ parametric images, as estimated on clipped sliding windows w, after normalization by the total signal power $E[\mu_w]$. This example corresponds to 0% SC (no attenuation). A lower average value indicates a higher level of red blood cell aggregation.

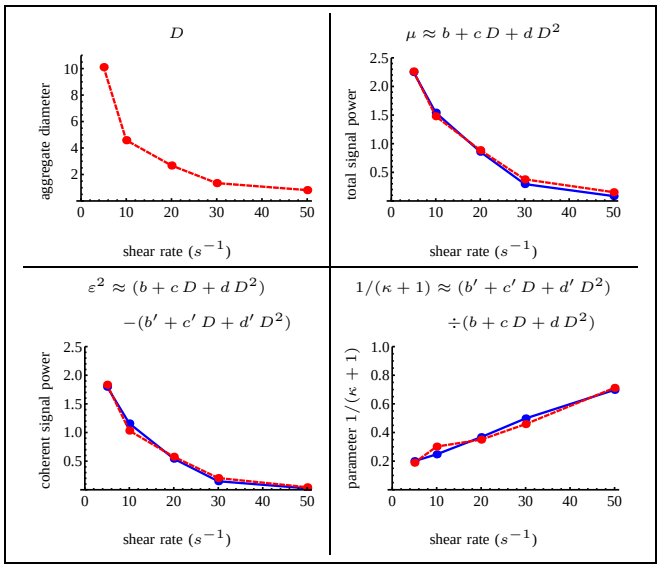

Fig. 4. QUS parameters for the data acquired without attenuation. *Top left:* The spectral parameter D (—), the mean isotropic aggregate diameter, as a function of shear rates (s^{-1}). Other graphs: Comparison of the total signal power μ, the coherent signal power ε^2 and the diffuse to total signal power ratio $1/(\kappa+1)$ of the MHK model estimated from the echo envelope of RF signals (—) with the corresponding rational or quadratic function of D (—) for five shear rates (s^{-1}).

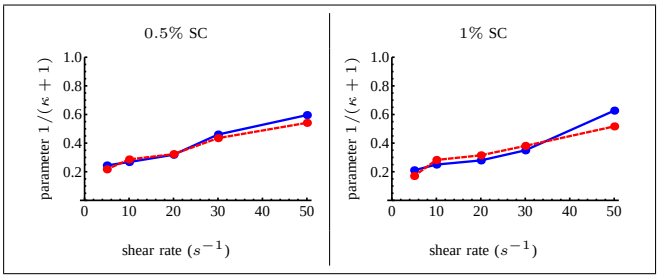

Fig. 5. Comparison of the diffuse to total signal power ratio $1/(\kappa+1)$ of the MHK model estimated from the echo envelope of RF signals (—) with the function $(b' + c'D + d'D^2)/(b + cD + dD^2)$ (—) of the isotropic aggregate diameter D for five shear rates (s^{-1}) and two levels of attenuation (expressed in % of SC).

$d' = -0.00926$, $b = -0.284$, $c = 0.469$, and $d = -0.0209$, assuming an uncertainty proportional to the response (*i.e.*, $1/(\kappa + 1)$ or μ) in the nonlinear fitting model. The spectral QUS parameter D, and the statistical MHK ones μ, ε^2 and $1/(\kappa+1)$ are represented in Fig. 4, as well as their expressions as a function of D. Good agreements can be observed.

Next, for each level of attenuation corresponding to 0.25%, 0.5%, 0.75%, and 1% SC, viewed as a testing set, estimated values of $1/(\kappa + 1)$ were compared with values of $(b' + c'D + d'D^2)/(b + cD + dD^2)$, where D was estimated with the SFSAE model. These values are reported in Table III, second to fifth rows. Resulting curves are represented in Fig. 5. Again, the good agreement between statistical and spectral-based results can be appreciated.

To further assess agreements between the diffuse to total signal power ratio and its expression in terms of D, a two-sided paired t-test showed that the choice of MHK or spectral method had no significant effect (p-value of 0.079) on estimates.

VII. Discussion

A. Mixtures of homodyned K-distributions

1) ROI segmentation: When there was almost no aggregation (corresponding to a shear rate of 50 s^{-1}), B-mode images presented a hypoechogenic aspect except for some small echogenic spots (representing 4% of the ROI area in the image of the top row of Fig. 1), which we think are due to small residual RBC aggregates. These spots were successfully detected by the proposed segmentation method. Moreover, considering averages E_{hypo} and E_{hyper} over the hypoechogenic and hyperechogenic segmented regions, respectively, ratios $E_{\text{hypo}}[(\mu_w - \varepsilon_w^2)]/E_{\text{hypo}}[\mu_w] = 0.75$ and $E_{\text{hyper}}[(\mu_w - \varepsilon_w^2)]/E_{\text{hyper}}[\mu_w] = 0.31$ were obtained (top row of Fig. 3), where w represents sliding windows as in Section VI-B, which is consistent with this interpretation. For higher levels of aggregation (corresponding to a shear rate ranging from 5 to 30 s^{-1}), B-mode images presented speckle spots with three different degrees of echogenicity (second and third rows of Fig. 1). We think that this is due to the polydispersity in aggregate sizes. Indeed, in these *in vitro* experiments on porcine blood, the Couette flow device provided a linear velocity profile and thus a constant shear rate, such that the rheology condition to promote or inhibit RBC aggregation was the same whatever the depth in the Couette annular space. However, for each shear rate, the blood sample may contain several sizes of aggregates mixed with disaggregated RBCs.

2) Statistical parameters: Although statistical parameters μ and ε^2 depend on attenuation (see Table III), it was shown

This article has been accepted for publication in a future issue of this journal, but has not been fully edited. Content may change prior to final publication. Citation information: DOI 10.1109/TMI.2015.2479455, IEEE Transactions on Medical Imaging

that the ratio $1/(\kappa+1) = (\mu-\varepsilon^2)/\mu$ was not affected by this variable.

B. Physical interpretation of the coherent component

Results of Section VI-B indicate that the coherent signal power ε^2 can be interpreted as the mean squared modulus of the local average IQ signal along the axial direction. The simpler interpretation of ε^2 as the modulus squared of $E[IQ]$ is not valid in the context of the present study. Indeed, the statistic $|E[IQ]|^2$ was computed directly on the data and turned out to represent less than 0.3% of the parameter ε^2. We think this is due to the fact that the local statistic $E_{\text{loc},z}[IQ]$ may be non-constant over the ROI, so that a global average $E[IQ] \approx E[E_{\text{loc},z}[IQ]]$ results in a lot of IQ signal canceling due to destructive wave interference.

C. Relations between the total and coherent signal powers and the SFSAE model

Based on [39], the SFSAE model can be expressed in terms of a single spectral parameter D, the isotropic aggregate diameter. The diffuse to total signal power ratio could be related explicitly to D, thus illustrating a relation between statistical and spectral approaches. In this model, the product $D2a$, where $2a$ is the diameter of one RBC, is the aggregate diameter estimate. A more recent BSC model, called the EMTSFM, was developed by our team [51]. Contrary to the scattering theory SFSAE, the EMTSFM provides a theoretical framework by considering aggregates as effective scatterers, so that the aggregate radius and the aggregate compactness intervene explicitly to parameterize the BSC. However, at the moment, only the SFSAE is used to assess RBC structural features in an inverse problem framework because the SFSAE model produces better fits to experimental BSC than the EMTSFM. The EMTSFM should consider incorporating polydispersity in aggregate sizes and compactnesses to provide an optimal model for the inversion of experimental data [52]. This is why we have only considered the simpler SFSAE model in this study.

D. Frequency range

Various recommendations for the frequency bandwidth have been proposed for reliable BSC estimates, based in particular on scatterers sizes. In the reported experimental tests, the spectral approach used the frequency bandwidth between 8 and 30 MHz [38], corresponding to a product ka below 0.34, where a is the RBC radius. For the proposed statistical approach, we recommend a same range as for the spectral approach; *i.e.*, a range for which BSC estimates are reliable in view of the interpretation given by Eqs (15) and (19). In particular, the various attenuation and diffraction compensation coefficients should be valid. Furthermore, if further hypotheses are made on the type of scattering (diffusion, diffraction, or reflection) in modeling the BSC, the corresponding range of ka should be assumed. Thus, it is understood that the instrumentation function $B(\omega)T(\omega)U(\omega)$ in Eq. (13) should be negligible outside the range in which the adopted BSC model is valid (possibly larger range after refinement of the model).

E. Relation with previous works

The pioneer work of [45], [53] related second-order statistics of the echo envelope to the BSC. In [37], an interpretation of the echo envelope intensity kurtosis based on the physics of the echo signal was presented, but in the special case of sparse monodisperse scatterers. In a more general setting, the backscattered power was related to the variance of local RBC concentrations [43], based on [48]. More recently, the scale and shape parameters of a generalized gamma distribution were proposed to quantify structural changes during cell death [54]. The point of view of considering the parameter $1/(\kappa+1)$ is akin to the approach introduced in [55] that identifies and removes non-diffuse echoes from the QUS analysis, as the assumption of diffuse scattering is not necessarily valid.

VIII. Conclusions

The following contributions were made in this paper:

1) Mixtures of homodyned K-distributions were proposed as a statistical model for the echo envelope of RF data of an ultrasound image, together with an estimation method.
2) Adopting Jakeman and Tough discretization of a continuous scattering model, in which the scattering medium was interpreted as a collection of local fluctuations in acoustical contrasts, MHK statistical parameters considered in point (1) could be related to two statistics of the IQ signal: the mean intensity and the mean squared modulus of the local average IQ signal along the axial direction.
3) Based on a physical model of ultrasound image formation, direct relations between statistics of the IQ signal considered in point (2), on one hand, and the instrumentation setting, tissue attenuation and the backscatter coefficient, on the other hand, were established.

To illustrate these concepts, RF data from *in vitro* experiments for various levels of RBC aggregation and skin-mimicking attenuation were analyzed with the proposed mixture model. In particular, it was shown that the diffuse to total signal power ratio of the MHK model is robust to attenuation and might be a useful quantity for measuring the level of red blood cell aggregation in an *in vivo* context, where attenuation occurs due to the presence of skin and other tissue layers. Furthermore, this MHK echo envelope statistical parameter was shown to be related to a spectral parameter, the SFSAE isotropic aggregate diameter D, with the advantage of requiring no reference phantom or attenuation estimation.

Concerning parametric images obtained by sliding windows [3], [6], one could also consider homodyned K-distribution parameters, such as the diffuse to total signal power ratio, as proposed in Section VI-B, in addition to the Nakagami m-parameter previously studied. The proposed parametric images, which are related to structural properties of underlying tissues (*i.e.*, the isotropic aggregate diameter D), could be a helpful diagnostic tool for clinicians. It would be interesting to further study this topic.

Although the RF signal contains the phase information (which is in principle lost in the echo envelope), it appears

This article has been accepted for publication in a future issue of this journal, but has not been fully edited. Content may change prior to final publication. Citation information: DOI 10.1109/TMI.2015.2479455, IEEE Transactions on Medical Imaging

that the structural organization of the echo signal backscattered by aggregated erythrocytes was nevertheless maintained in the echo envelope in the reported tests. The same conclusion was reached by [37] in the case of sparse scatterers of small sizes. This observation should be assessed for other biological tissues.

Furthermore, although single-element transducers were considered in this work, we expect that the theoretical framework can be adapted to linear-array transducers.

As a final remark, we expect the physical interpretation introduced in the present study to hold for biological tissues other than aggregated erythrocytes, under the hypothesis of Born approximation, although this statement remains to be validated. In the presence of specular reflections (*e.g.*, due to calcium in atherosclerotic plaques), such an interpretation would have to be adjusted by modifying the BSC model accordingly. Related to this issue, although in the current work scatterers were modeled as forming a random process, one could also consider structured organization of quasi or pseudo-periodic alignment of scatterers, as in [16], [20], [56]. Also, note that in the framework of [35], the structure factor model at the origin of the SFSAE was shown to be valid and better than state-of-the-art modeling approaches in the case of cancer cell pellets. This is also supporting the validity of unifying concepts presented in this study for other biological tissues than blood.

REFERENCES

[1] P. M. Shankar, J. M. Reid, H. Ortega, C. W. Piccoli, and B. B. Goldberg, "Use of non-Rayleigh statistics for the identification of tumors in ultrasonic B-scans of the breast," *IEEE Trans. Med. Imag.*, vol. 12, no. 4, pp. 687–692, 1993.

[2] P. M. Shankar, V. A. Dumane, J. M. Reid, V. Genis, F. Forsberg, C. W. Piccoli, and B. B. Goldberg, "Classification of ultrasonic B-mode images of breast masses using Nakagami distribution," *IEEE Trans. Ultrason. Ferroelectr. Freq. Control.*, vol. 48, no. 2, pp. 569–580, 2001.

[3] P.-H. Tsui, Y.-Y. Liao, C.-C. Chang, W.-H. Kuo, K.-J. Chang, and C.-K. Yeh, "Classification of benign and malignant breast tumors by 2-d analysis based on contour description and scatterer characterization," *IEEE Trans. Med. Imag.*, vol. 29, no. 2, pp. 513–522, 2010.

[4] J. Mamou, A. Coron, M. L. Oelze, E. Saegusa-Beecroft, M. Hata, P. Lee, J. Machi, E. Yanagihara, P. Laugier, and E. J. Feleppa, "Three-dimensional high-frequency backscatter and envelope quantification of cancerous human lymph nodes," *Ultrasound Med. Biol.*, vol. 37, no. 3, pp. 2055–2068, 2011.

[5] I. Trop, F. Destrempes, M. El Khoury, A. Robidoux, L. Gaboury, L. Allard, B. Chayer, and G. Cloutier, "The added value of statistical modeling of backscatter properties in the management of breast lesions at ultrasound," *Radiology*, vol. 275, no. 3, pp. 666–674, 2015.

[6] A. Larrue and J. A. Noble, "Modeling of errors in Nakagami imaging: Illustration on breast mass characterization," *Ultrasound Med. Biol.*, vol. 40, no. 5, pp. 917–930, 2014.

[7] I. B. Hampshire II, *A non-Rayleigh model for ultrasonic backscatter myocardium"*. Master's Thesis, Thayer School of Engineering, Darmouth College, 1988.

[8] L. Clifford, P. Fitzgerald, and D. James, "Non-Rayleigh first-order statistics of ultrasonic backscatter from normal myocardium," *Ultrasound Med. Biol.*, vol. 19, no. 6, pp. 487–495, 1993.

[9] X. Hao, C. J. Bruce, C. Pislaru, and J. F. Greenleaf, "Characterization of reperfused infarcted myocardium from high-frequency intracardiac ultrasound imaging using homodyned K distribution," *IEEE Trans. Ultrason. Ferroelectr. Freq. Control*, vol. 49, no. 11, pp. 1530–1542, 2002.

[10] J. C. Seabra, F. Ciompi, O. Pujol, J. Mauri, P. Radeva, and J. Sanches, "Rayleigh mixture model for plaque characterization in intravascular ultrasound," *IEEE Trans. Biomed. Eng.*, vol. 58, no. 5, pp. 1314–1324, 2011.

[11] G. Vegas-Sánchez-Ferrero, J. Seabra, O. Rodriguez-Leor, A. Serrano-Vida, S. Aja-Fernández, M. Martín-Fernández, C. Palencia, and J. Sanches, "Gamma mixture classifier for plaque detection in intravascular ultrasonic images," *IEEE Trans. Ultrason. Ferroelectr. Freq. Control.*, vol. 61, no. 1, pp. 44–61, 2014.

[12] D. Sheet, A. Karamalis, A. Eslami, P. Noël, J. Chatterjee, A. K. Ray, A. F. Laine, S. G. Carlier, N. Navab, and A. Katouzian, "Joint learning of ultrasonic backscattering statistical physics and signal confidence primal for characterizing atherosclerotic plaques using intravascular ultrasound," *Med. Image Analysis*, vol. 18, no. 1, pp. 103–117, 2014.

[13] T. Yamaguchi, "The quantitative ultrasound diagnosis of liver fibrosis using statistical analysis of the echo envelope," in *Quantitative Ultrasound in Soft Tissues*, J. Mamou and M. L. Oelze, Eds. Springer Dordrecht Heidelberg New York London, 2013, pp. 275–290.

[14] A. I. L. Namburete, B. Rahmatullah, and J. A. Noble, "Nakagami-based AdaBoost learning framework for detection of anatomical landmarks in 2D detal neurosonograms," *Annals of the BMVA*, vol. 2013, no. 2, pp. 1–16, 2013.

[15] E. Jakeman and R. J. A. Tough, "Generalized *k* distribution: a statistical model for weak scattering," *J. Opt. Soc. Am. A*, vol. 4, pp. 1764–1772, 1987.

[16] V. Dutt and J. F. Greenleaf, "Ultrasound echo envelope analysis using a homodyned k distribution signal model," *Ultrasonic Imaging*, vol. 16, no. 4, pp. 265–287, 1994.

[17] F. Destrempes and G. Cloutier, "Review of envelope statistics models for quantitative ultrasound imaging and tissue characterization," in *Quantitative Ultrasound in Soft Tissues*, J. Mamou and M. L. Oelze, Eds. Springer Dordrecht Heidelberg New York London, 2013, pp. 219–274.

[18] P. M. Shankar, "A general statistical model for ultrasonic backscattering from tissues," *IEEE Trans. Ultrason. Ferroelectr. Freq. Control.*, vol. 47, no. 3, pp. 727–736, 2000.

[19] F. Destrempes and G. Cloutier, "A critical review and uniformized representation of statistical distributions modeling the ultrasound echo envelope," *Ultrasound Med. Biol.*, vol. 36, no. 7, pp. 1037–1051, 2010.

[20] P. M. Shankar, "A model for ultrasonic scattering from tissues based on the k distribution," *Phys. Med. Biol.*, vol. 40, no. 10, pp. 1633–1649, 1995.

[21] F. L. Lizzi, M. Greenebaum, E. J. Feleppa, and M. Elbaum, "Theoretical framework for spectrum analysis in ultrasonic tissue characterization," *J. Acoust. Soc. Am.*, vol. 73, no. 4, pp. 1366–1373, 1983.

[22] F. L. Lizzi, M. Ostromogilsky, E. J. Feleppa, M. C. Rorke, and M. M. Yaremko, "Relationship of ultrasonic spectral parameters to features of tissue microstructure," *IEEE Trans. Ultrason. Ferroelectr. Freq. Control.*, vol. 34, no. 3, pp. 319–329, 1987.

[23] M. C. Kolios, G. J. Czarnota, M. Lee, J. W. Hunt, and M. D. Sherar, "Ultrasonic spectral parameter characterization of apoptosis," *Ultrasound Med. Biol.*, vol. 28, no. 5, pp. 589–597, 2002.

[24] E. J. Feleppa, F. L. Lizzi, D. J. Coleman, and M. M. Yaremko, "Diagnostic spectrum analysis in ophthalmology: A physical perspective," *Ultrasound Med. Biol.*, vol. 12, no. 8, pp. 623–631, 1986.

[25] E. J. Feleppa, T. Liu, A. Kalisz, M. C. Shao, N. Fleshner, and V. Reuter, "Ultrasonic spectral-parameter imaging of the prostate," *Int. J. Imaging Syst. Technol.*, vol. 8, no. 1, pp. 11–25, 1997.

[26] M. L. Oelze, J. F. Zachary, and W. D. O'Brien, Jr., "Characterization of tissue microstructure using ultrasonic backscatter: Theory and technique for optimization using a Gaussian form factor," *J. Acoust. Soc. Am.*, vol. 112, no. 3 Pt 1, pp. 1202–1211, 2002.

[27] M. L. Oelze, W. D. O'Brien, Jr., J. P. Blue, and J. F. Zachary, "Differentiation and characterization of rat mammary fibroadenomas and 4T1 mouse carcinomas using quantitative ultrasound imaging," *IEEE Trans. Med. Imag.*, vol. 23, no. 6, pp. 764–771, 2004.

[28] J. Mamou, A. Coron, M. Hata, J. Machi, E. Yanagihara, P. Laugier, and E. Feleppa, "Three-dimensional high-frequency characterization of cancerous lymph nodes," *Ultrasound Med. Biol.*, vol. 36, no. 3, pp. 361–375, 2010.

[29] F. T. H. Yu and G. Cloutier, "Experimental ultrasound characterization of red blood cell aggregation using the structure factor size estimator," *J. Acoust. Soc. Am.*, vol. 122, no. 1, pp. 645–656, 2007.

[30] R. M. Vlad, R. K. Saha, N. M. Alajez, S. Ranieari, G. J. Czarnota, and M. C. Kolios, "An increase in cellular size variance contributes to the increase in ultrasound backscatter during cell death," *Ultrasound Med. Biol.*, vol. 36, no. 9, pp. 1546–1558, 2010.

[31] A. Han, R. Abuhabsah, R. J. Miller, S. Sarwate, and W. D. O'Brien, Jr, "The measurement of ultrasound backscattering from cell pellet biophantoms and tumors ex vivo," *J. Acoust. Soc. Am.*, vol. 134, no. 1, pp. 686–693, 2013.

This article has been accepted for publication in a future issue of this journal, but has not been fully edited. Content may change prior to final publication. Citation information: DOI 10.1109/TMI.2015.2479455, IEEE Transactions on Medical Imaging

[32] D. Savéry and G. Cloutier, "A point process approach to assess the frequency dependence of ultrasound backscattering by aggregating red blood cells," *J. Acoust. Soc. Am.*, vol. 110, no. 6, pp. 3252–3262, 2001.
[33] I. Fontaine, D. Savéry, and G. Cloutier, "Simulation of ultrasound backscattering by red blood cell aggregates: effect of shear rate and anisotropy," *Biophys. J.*, vol. 82, no. 4, pp. 1696–1710, 2002.
[34] E. Franceschini and R. Guillermin, "Experimental assessment of four ultrasound scattering models for characterizing concentrated tissue-mimicking phantoms," *J. Acoust. Soc. Amer.*, vol. 132, no. 6, pp. 3735–3747, 2012.
[35] E. Franceschini, R. Guillermin, F. Tourniaire, S. Roffino, E. Lamy, and J.-F. Landrier, "Structure Factor Model for understanding the measured backscatter coefficients from concentrated cell pellet biophantoms," *J. Acoust. Soc. Amer.*, vol. 135, no. 6, pp. 3620–3631, 2014.
[36] A. Han and W. D. O'Brien, Jr, "Structure function for high-concentration biophantoms of polydisperse scatterer sizes," *IEEE Trans. Ultrason. Ferroelectr. Freq. Control.*, vol. 62, no. 2, pp. 303–318, 2015.
[37] J.-F. Chen, J. A. Zagzebski, and E. L. Madsen, "Non-Gaussian versus non-Rayleigh statistical properties of ultrasound echo signals," *IEEE Trans. Ultrason. Ferroelectr. Freq. Control.*, vol. 41, no. 4, pp. 435–440, 1994.
[38] E. Franceschini, F. T. H. Yu, F. Destrempes, and G. Cloutier, "Ultrasound characterization of red blood cell aggregation with intervening attenuating tissue-mimicking phantoms," *J. Acoust. Soc. Am.*, vol. 127, no. 2, pp. 1104–1115, 2010.
[39] R. K. Saha, E. Franceschini, and G. Cloutier, "Assessment of accuracy of the structure-factor-size-estimator method in determining red blood cell aggregate size from ultrasound spectrum backscattering coefficient," *J. Acoust. Soc. Am.*, vol. 129, no. 4, pp. 2269–2277, 2011.
[40] F. Destrempes, J. Porée, and G. Cloutier, "Estimation method of the homodyned K-distribution based on the mean intensity and two log-moments," *SIAM J. Imaging Sciences*, vol. 6, no. 3, pp. 1499–1530, 2013.
[41] F. Destrempes, J. Meunier, M.-F. Giroux, G. Soulez, and G. Cloutier, "Segmentation in ultrasonic B-mode images of healthy carotid arteries using mixtures of Nakagami distributions and stochastic optimization," *IEEE Trans. Med. Imag.*, vol. 28, no. 2, pp. 215–229, 2009.
[42] L. Weng, J. M. Reid, P. M. Shankar, and K. Soetanto, "Ultrasound speckle analysis based on the K distribution," *J. Acoust. Soc. Am.*, vol. 89, no. 6, pp. 2992–2995, 1991.
[43] L. Y. L. Mo and R. S. C. Cobbold, "A unified approach to modeling the backscattered Doppler ultrasound from blood," *IEEE Trans. Biomed. Eng*, vol. 39, no. 5, pp. 450–461, 1992.
[44] F. W. Steutel and M. J. A. Van Eenige, "Note on the approximation of distributions on z+ by mixtures of negative binomial distributions," *Commun. Statist. Stochastic Models*, vol. 13, no. 2, pp. 271–274, 1997.
[45] M. F. Insana, R. F. Wagner, D. G. Brown, and T. J. Hall, "Describing small-scale structure in random media using pulse-echo ultrasound," *J. Acoust. Soc. Am.*, vol. 87, no. 1, pp. 179–192, 1990.
[46] M. F. Insana, T. J. Hall, and L. T. Cook, "Backscatter coeffcient estimation using array transducers," *IEEE Trans. Ultrason. Ferroelectr. Freq. Control.*, vol. 41, no. 5, pp. 714–723, 1994.
[47] D. A. Greenwood, "The asymptotic form of the structure factor for simple liquids," *J. Phys. C: Solid St. Phys.*, vol. 33, pp. 331–334, 1980.
[48] V. Twersky, "Low-frequency scattering by correlated distributions of randomly oriented particles," *J. Acoust. Soc. Am.*, vol. 81, no. 7, pp. 1609–1618, 1987.
[49] W. J. Dixon, "Simplified estimation from normal samples," *Ann. Math. Stat.*, vol. 31, pp. 385–391, 1960.
[50] D. P. Hruska, J. R. Sanchez, and M. L. Oelze, "Improved diagnostics through quantitative ultrasound imaging," in *IEEE Conf. Eng. Med. Biol. Soc.*, 2009, pp. 1956–1959.
[51] E. Franceschini, B. Metzger, and G. Cloutier, "Forward problem study of an effective medium model for ultrasound blood characterization," *IEEE Trans. Ultrason. Ferroelectr. Freq. Control.*, vol. 58, no. 12, pp. 2668–2679, 2011.
[52] E. Franceschini, R. K. Saha, and G. Cloutier, "Comparison of three scattering models for ultrasound blood characterization," *IEEE Trans. Ultrason. Ferroelectr. Freq. Control.*, vol. 60, no. 11, pp. 2321–2334, 2013.
[53] M. F. Insana, R. F. Wagner, B. S. Garra, D. G. Brown, and T. H. Shawker, "Analysis of ultrasound image texture via generalized Rician statistics," *Opt. Eng.*, vol. 25, no. 6, pp. 743–748, 1986.
[54] A. S. Tunis, G. J. Czarnota, A. Giles, M. D. Sherar, J. W. Hunt, and M. C. Kolios, "Monitoring structural changes in cells with highfrequency ultrasound signal statistics," *Ultrasound Med. Biol.*, vol. 31, no. 8, pp. 1041–1049, 2005.
[55] A. C. Luchies, G. Ghoshal, W. D. O'Brien, Jr., and M. L. Oelze, "Quantitative ultrasonic characterization of diffuse scatterers in the presence of structures that produce coherent echoes," *IEEE Trans. Ultrason. Ferroelectr. Freq. Control.*, vol. 59, no. 5, pp. 893–904, 2012.
[56] J. W. Hunt, A. E. Worthington, A. Xuan, M. C. Kolios, G. J. Czarnota, and M. D. Sherar, "A model based upon pseudo regular spacing of cells combined with the randomisation of the nuclei can explain the significant changes in high-frequency ultrasound signals during apoptosis," *Ultrasound Med. Biol.*, vol. 28, no. 2, pp. 217–226, 2002.
[57] S. Geman and D. Geman, "Stochastic relaxation, Gibbs distributions and the Bayesian restoration of images," *IEEE Trans. Pattern Analysis and Machine Intelligence*, vol. 6, no. 6, pp. 721–741, 1984.
[58] J. Maroquin, S. Mitter, and T. Poggio, "Probabilistic solution of ill-posed problems in computation vision," *J. Am. Statistical Assoc.*, vol. 82, no. 397, pp. 76–89, 1987.
[59] H. Teicher, "Identifiability of finite mixtures," *Ann. Math. Statist.*, vol. 34, no. 4, pp. 1147–1659, 1963.
[60] M. Abramowitz and I. A. Stegun, Eds., *Handbook of Mathematical Functions with Formulas, Graphs, and Mathematical Tables*. New York: Dover, 1972.

APPENDIX A: SEGMENTATION ALGORITHM

The proposed segmentation method is based on a Markov random field (MRF) model. For each pixel s of the ROI, the discrete variable z_s denotes the region class of the pixel, so that $z_s \in \{1, 2, ..., \ell\}$, where ℓ is the maximal number of distributions in the mixture, and A_s denotes the amplitude of the echo envelope at that pixel. The vector of variables $\mathbf{z} = (z_s)$ is viewed as a hidden discrete random field on the lattice of pixels of the ROI. The vector of variables $\mathbf{A}_{\text{MRF}} = (A_s)$ is viewed as a continuous random field and is observable, whereas z has to be estimated from the data. Conditional to each class $j = 1, 2, ..., \ell$, a Nakagami distribution model [7] was adopted, with parameters m_j (the shape parameter) and Ω_j (the scaling parameter). Assuming, as is commonly done in image processing [57], that amplitudes are independent conditional to the region labeling of pixels, one obtains the likelihood of the MRF model in the form of a product of pixel-based likelihoods. For the prior on the labeling $\mathbf{z}$, a simple Potts model [57] was adopted, based on vertical and horizontal neighbors of pixels. Altogether, one obtains the joint distribution of the proposed MRF model as the product of the likelihood and the prior.

In the reported tests, ℓ was set equal to 3. The parameters $(m_j,\ \Omega_j)$, $j = 1, 2, ..., \ell$, were estimated on the ROI by the Expectation-Maximization (EM) algorithm adapted to mixtures of Nakagami distributions in [41, Table I]. Ten random initializations of the EM were used in our implementation, each one obtained with the K-means algorithm. Then, knowing these parameters, the Modes of Posterior Marginals (MPM) algorithm [58] was applied to classify pixels in the ROI. Namely, for each pixel s, the region label z_s was chosen as the one that maximized the posterior marginal $P(z_s \mid \mathbf{A}_{\text{MRF}}, (z_r)_{r \neq s})$. Algorithmically, we used the Gibbs sampler [57] to simulate the posterior distribution $P(z | \mathbf{A}_{\text{MRF}})$ based on the posterior marginals. One then approximated the mode $\arg\max_{z_s} P(z_s \mid \mathbf{A}_{\text{MRF}}, (z_r)_{r \neq s})$ at each pixel s as the most frequent label z_s that occurred at s within the Gibbs sampling of the posterior distribution. The MPM algorithm was initialized with one random initialization of pixel labels. The first 50 iterations of the Gibbs sampling were discarded (the so-called burn-in period) and then, 50 more iterations

This article has been accepted for publication in a future issue of this journal, but has not been fully edited. Content may change prior to final publication. Citation information: DOI 10.1109/TMI.2015.2479455, IEEE Transactions on Medical Imaging

were used for the estimation of the MPM. To speed up the MPM algorithm, the likelihoods $P(A_s|z_s)$ were pre-computed before the first iteration and stored in a lookup table based on a discretization of A_s into 1200 bins.

Appendix B: Identifiability of finite mixtures of homodyned K-distributions

The following result states the identifiability of finite mixtures of homodyned K-distributions. The idea of its proof is to use Hankel transform in a variant of Teicher's approach [59].

Theorem 1: *Assume that*

$$\sum_{j=1}^{\ell} p_j P_{HK}(A \mid \varepsilon_j, \sigma_j^2, \alpha_j) = \sum_{j=1}^{\ell'} \tilde{p}_j P_{HK}(A \mid \tilde{\varepsilon}_j, \tilde{\sigma}_j^2, \tilde{\alpha}_j) \quad (25)$$

for all $A > 0$, where $p_j > 0$ ($j = 1, ..., \ell$) and $\tilde{p}_j > 0$ ($j = 1, ..., \ell'$). Assume also that $(\varepsilon_j, \sigma_j, \alpha_j) \neq (\varepsilon_{j'}, \sigma_{j'}, \alpha_{j'})$ for any $j \neq j'$, and similarly for the other mixture. Then, $\ell = \ell'$ and up to permutation of indices, $p_j = \tilde{p}_{j'}$ and $(\varepsilon_j, \sigma_j^2, \alpha_j) = (\tilde{\varepsilon}_j, \tilde{\sigma}_j^2, \tilde{\alpha}_j)$ for $j = 1, ..., \ell$.

Proof: We proceed in the following steps.

Step 1. Let Eq. (25) hold for all $A > 0$, with the assumptions of Theorem 1. Reordering the distributions of each mixture if necessary, we may assume that $\varepsilon_1 \geq \varepsilon_2 \geq ... \geq \varepsilon_\ell$, as well as $\tilde{\varepsilon}_1 \geq \tilde{\varepsilon}_2 \geq ... \geq \tilde{\varepsilon}_{\ell'}$.

Step 2. To each probability density function P on $A > 0$ is associated the Hankel transform $\phi(u)$, of order 0, of the function $P(A)/A$; that is $\int_0^\infty J_0(uA)P(A)\,dA$. This defines a linear operator M. For the homodyned K-distribution distribution, one obtains the Hankel transform

$$\phi(u) = J_0(u\varepsilon)\Big(1 + u^2\frac{\sigma^2}{2}\Big)^{-\alpha} \quad (26)$$

defined for any $u > 0$. This follows from Eq. (1) using the closure equation $\int_0^\infty J_0(vA)J_0(uA)A\,dA = \frac{\delta(v-u)}{u}$, where δ denotes the Dirac delta distribution.

The function $\phi(u)$ can be extended to an analytic function $\psi(z)$ defined on the open subset

$$U = \{z\ : -\frac{\pi}{4} < \arg(z) < \frac{\pi}{2}\} \quad (27)$$

of the complex plane $\mathbb{C}$. Indeed, the function $J_0(z\varepsilon)$ is an entire function [60, (9.1.10)]. Moreover, the function $1+z^2\frac{\sigma^2}{2}$ maps U into the open set $V = \{w\ : -\frac{\pi}{2} < \arg(w-1) < \pi\}$; then, the branch of the logarithm defined on $V \subset \mathbb{C}\backslash i(-\infty, 0]$ can be applied to obtain $(1 + z^2\frac{\sigma^2}{2})^{-\alpha}$.

The function $\psi(z)$ can be extended to a strip

$$U_t' = \{w\ :\ |\Re(w)| < 1/2 \text{ and } \Im(w) > t\}, \quad (28)$$

where $t \geq \frac{2}{\sigma^2}$. Then, based on the Taylor expansion of $(1 + z^{-2}\frac{2}{\sigma^2})^{-\alpha}$, valid for large values of $|z|$, one computes at $z = iu$, with $u > 0$:

$$\psi(iu) = I_0(u\varepsilon)\Big(-u^2\frac{\sigma^2}{2}\Big)^{-\alpha}\sum_{k=0}^{\infty}\frac{(k+\alpha-1)!}{k!(\alpha-1)!}\Big(u^2\frac{\sigma^2}{2}\Big)^{-k}, \quad (29)$$

where we have used [60, (9.6.3)].

Step 3. By linearity of the operator M, we deduce from steps 1 and 2 the identity

$$\Psi(z) = \sum_{j=1}^{\ell} p_j\psi_j(z) = \sum_{j=1}^{\ell'}\tilde{p}_j\tilde{\psi}_j(z) \quad (30)$$

for all $z \in U \cup U_t'$, taking t sufficiently large.

Now, let $\varepsilon_1 = \varepsilon_2 = ... = \varepsilon_r$, with $1 \leq r \leq \ell$ maximal with this property (*i.e.*, $r = \ell$ or $\varepsilon_r > \varepsilon_{r+1}$). Consider $z = iu \in U_t'$. Let $\Lambda = \{\alpha_j + k\ :\ 1 \leq j \leq r \text{ and } k \in \mathbb{N}\}$ and let $\lambda_1, \lambda_2, ...$ be an enumeration of Λ in increasing order. From Eq. (29), we can write $\Psi(iu)$ in the form

$$\Psi(iu) = I_0(u\varepsilon_1)\sum_{n=1}^{\infty} c_n\Big(u^2\frac{\sigma^2}{2}\Big)^{-\lambda_n} + \Psi'(iu), \quad (31)$$

where $\Psi'(iu) = 0$ (if $r = \ell$) or $\Psi'(iu) = \sum_{j=r+1}^{\ell} p_j\psi_j(iu)$ (if $r < \ell$) and the c_n's are real coefficients. Here, we have dropped all coefficients c_n that vanish (if any). Based on the asymptotic expansion [60, (9.7.1)] $I_0(u\varepsilon) \sim \frac{e^{u\varepsilon}}{\sqrt{2\pi u\varepsilon}}$, valid for large values of $u > 0$, we deduce from Eqs. (26) and (31) that

$$\lim_{u\to\infty}\frac{\Psi(iu)}{I_0(u\varepsilon)u^{-2\lambda}} = 0;\ \lim_{u\to\infty}\frac{\Psi(iu)}{I_0(u\varepsilon_1)u^{-2\lambda_1}} = c_1 \neq 0, \quad (32)$$

where the first equality holds whenever $\varepsilon > \varepsilon_1$, or $\varepsilon = \varepsilon_1$ and $\lambda < \lambda_1$. It follows that ε_1, λ_1 and c_1 are determined by $\Psi(z)$. Then, arguing by induction, we obtain that

$$\Psi_N(iu) = I_0(u\varepsilon_1)\sum_{n=N}^{\infty} c_n\big(u^2\frac{\sigma^2}{2}\big)^{-\lambda_n} + \Psi'(iu) \quad (33)$$

satisfies the conditions

$$\lim_{u\to\infty}\frac{\Psi_N(iu)}{I_0(u\varepsilon_1)u^{-2\lambda}} = 0;\ \lim_{u\to\infty}\frac{\Psi_N(iu)}{I_0(u\varepsilon_1)u^{-2\lambda_N}} = c_N \neq 0, \quad (34)$$

where $\lambda < \lambda_N$ for the first identity. Therefore, all values of λ_n and c_n are determined by $\Psi(z)$. It follows that $\varepsilon_1 = \tilde{\varepsilon}_1$ and

$$\sum_{j=1}^{r} p_j\big(1 + z^2\frac{\sigma_j^2}{2}\big)^{-\alpha_j} = \sum_{j=1}^{r'}\tilde{p}_j\big(1 + z^2\frac{\tilde{\sigma}_j^2}{2}\big)^{-\tilde{\alpha}_j} \quad (35)$$

for all z in U_t', and hence in U.

Step 4. Consider the relation "$\prec$" (similar to [59]) defined by: $(\sigma^2, \alpha) \prec (\hat{\sigma}^2, \hat{\alpha})$ if and only if 1) $\sigma^2 > \hat{\sigma}^2$; or 2) $\sigma^2 = \hat{\sigma}^2$ and $\alpha > \hat{\alpha}$. The condition $(\sigma^2, \alpha) \prec (\hat{\sigma}^2, \hat{\alpha})$ implies that

$$\lim_{z\to i\sqrt{2/\sigma^2}}\frac{(1 + z^2\frac{\hat{\sigma}^2}{2})^{-\hat{\alpha}}}{(1 + z^2\frac{\sigma^2}{2})^{-\alpha}} = 0. \quad (36)$$

Let (σ_j^2, α_j), $j = 1, ..., r$, be labeled by increasing order with respect to the relation $\prec$. Arguing as in [59], it follows that $r = r'$, and $p_j = \tilde{p}_j$, $\sigma_j^2 = \tilde{\sigma}_j^2$ and $\alpha_j = \tilde{\alpha}_j$, for $j = 1, ..., r$. From step 3, we also have $\varepsilon_j = \tilde{\varepsilon}_j$, for $j = 1, ..., r$.

Step 5. We consider again the identity (30) valid for all $z \in U \cup U_t'$. From step 4, we deduce that

$$\sum_{j=r+1}^{\ell} p_j\psi_j(z) = \sum_{j=r+1}^{\ell'}\tilde{p}_j\tilde{\psi}_j(z). \quad (37)$$

This article has been accepted for publication in a future issue of this journal, but has not been fully edited. Content may change prior to final publication. Citation information: DOI 10.1109/TMI.2015.2479455, IEEE Transactions on Medical Imaging

Arguing by induction on the number of distributions in the mixtures, there remains two possibilities: 1) $\ell = \ell'$ and the conclusion of Theorem 1 is reached; or 2) $\ell \neq \ell'$. We now rule out the second possibility. Assuming without loss of generality that $\ell > \ell'$, then, we obtain $\sum_{j=\ell'+1}^{\ell} p_j \psi_j(z) = 0$. But this implies that $\lim_{z\to 0} \sum_{j=\ell'+1}^{\ell} p_j \psi_j(z) = \sum_{j=\ell'+1}^{\ell} p_j = 0$, which is a contradiction. Thus, it must be that $\ell = \ell'$ and the proof of Theorem 1 is completed. ■